

UC Irvine

UC Irvine Previously Published Works

Title

Lattice engineering through nanoparticle-DNA frameworks

Permalink

<https://escholarship.org/uc/item/6f40t0hq>

Journal

Nature Materials, 15(6)

ISSN

1476-1122

Authors

Tian, Ye
Zhang, Yugang
Wang, Tong
et al.

Publication Date

2016-06-01

DOI

10.1038/nmat4571

Peer reviewed



HHS Public Access

Author manuscript

Nat Mater. Author manuscript; available in PMC 2017 January 31.

Published in final edited form as:

Nat Mater. 2016 June ; 15(6): 654–661. doi:10.1038/nmat4571.

Lattice Engineering via Nanoparticle-DNA Frameworks

Ye Tian¹, Yugang Zhang¹, Tong Wang², Huolin L. Xin¹, Huilin Li^{2,3}, and Oleg Gang^{1,*}

¹Center for Functional Nanomaterials, Brookhaven National Laboratory, Upton, NY 11973, USA

²Biosciences Department, Brookhaven National Laboratory, Upton, New York 11973, USA

³Department of Biochemistry and Cell Biology, Stony Brook University, Stony Brook, New York 11794, USA

Abstract

Advances in self-assembly over the last decade have demonstrated that nano- and microscale particles can be organized into a large diversity of ordered three-dimensional (3D) lattices. However, the ability to generate the desired lattice type from the same set of particles remains challenging. Here, we show that nanoparticles can be assembled into crystalline and open 3D frameworks by connecting them through designed DNA-based polyhedral frames. The well-defined geometrical shapes of the frames, combined with the DNA-assisted binding properties of their vertices, facilitate the well-defined topological connections between particles in accordance with frame geometry. With this strategy, different crystallographic lattices using the same particles can be assembled by introduction of the corresponding DNA polyhedral frames. This approach should facilitate the rational assembly of nanoscale lattices through the design of the unit cell.

The progress in nano-material fabrication methods was for long time motivated by the idea that self-assembly will endow us with ability to organize nanoparticles in the designed arrays. In reality, the particle characteristics have a profound effect on the assembled structure, thus, a little room is remaining for a structure architecting. Yet, it would be far more powerful to have an ability generating the different desired types of 3D lattices from the same particles. Such freedom of lattice engineering will permit fabricating targeted materials, which properties can be enhanced and manipulated by precise organization of functional components^{1–5}.

Colloids, often presented as a model of atomic systems, have revealed a great insight about the fundamentals of crystal formation^{6–9} and the role of a particle nature^{10–12}. Although an

Reprints and permissions information is available online at www.nature.com/reprints.

*Correspondence and requests for materials should be addressed to O.G., ogang@bnl.gov.

Author contributions

Y.T. and O.G. conceived and designed the experiments. Y.T. performed the experiments. Y.Z. contributed to the model fitting of the SAXS data. Y.T., T.W. and H.L. contributed to the cryo-EM imaging and reconstruction. Y.T. and H.X. contributed to the STEM imaging of the superlattice. Y.T., Y.Z. and O.G. analysed the data. Y.T. and O.G. wrote the paper. O.G. supervised the project. All authors discussed the results and commented on the manuscript.

Supplementary information is available in the online version of the paper.

Competing financial interests

The authors declare no competing financial interests.

extremely rich variety of lattices have been demonstrated^{12–15}, the particular particle characteristics—such as sizes^{13,16,17}, interactions, entropic and many-body effects^{18–21}, and shape^{22–24}—dominate lattice formation. These dependencies are both natural and useful; numerous investigations have detailed how particle characteristics drive structure formation^{12,24–28}. While these studies uncovered a great depth of physical insight, the goal of lattice “engineering” remains elusive, due to the complex dependences between the structural and energetic parameters of particle and lattice, and the necessity to tailor particles for each target lattice.

Anisotropic interparticle interactions, induced by precise arrangement of binding patches or by particle shaping, were considered as means to simplify the lattice design. These particles have been extensively investigated for regulating phase formation^{11,29,30}, and diverse phases were predicted²⁹. Several recent studies exploited directional interactions to create particles clusters and arrays^{13,31–34}. However, such approaches require ample efforts in fabrication of building blocks with sophisticated anisotropic interactions. High-fidelity and high-yield fabrication of these elaborate particles remains challenging, particularly on the nanoscale^{32,35–37}. Besides, the resultant lattices are still determined by the specific particle design. DNA-based methods have emerged as a powerful approach for 3D crystallization^{14,15,38}, where phases can be controlled via particle size, shape, tailoring of DNA shells^{23,33}, and even in dynamic manner by selective interaction triggering³⁹. Despite these significant advances, assembled phases remain determined by particle details. Here, we propose a conceptually different approach, in which we shift the problem of lattice design from tailoring nanoscale particles, into forcing the connection between isotropic particles by precisely engineered anisotropic linkages. Specifically, polyhedral 3D DNA-origami^{40,41} frames, whose vertices connect DNA-encoded nanoparticles^{42,43} (NPs), facilitate the establishment of local particles coordination that results in the formation of 3D ordered nanoparticle-DNA frameworks (Fig. 1). We demonstrate that the same kind of NPs can be assembled into different types of lattices by employing appropriately designed polyhedral frames. Moreover, the crystallographic type of the assembled lattice (framework) is correlated with the frame geometry. Thus, our strategy potentially permits the deliberate engineering of the unit cell by controlling the shape of the particle-connecting frames and does not require particle modifications. This approach addresses the challenge articulated by Ned Seaman in his visionary work, more than three decades ago, that led to the rise of the field of DNA nanotechnology⁴⁴: how to create 3D lattices that position guest species in a predetermined, regular manner?

In this work, we designed⁴⁵ five different DNA origami polyhedral frames, including octahedron, cube, elongated square bipyramid (ESB), prism and triangular bipyramid (TBP), built using six-helix-bundle edges with the length (depending on the frame shape) from 30 to 45 nm, as shown in Fig. 1 and detailed in supplemental materials. Every bundle has one single-stranded DNA chain extending from each of its both ends. This chain can further hybridize with complementary DNA, which coat NPs uniformly. Thus, for all our designs, the number of strands linking a frame vertex to an individual NP is equal to the number of edges at the given vertex. The designed DNA frames thus connect NPs at their vertices, establishing the overall lattice topology based on frame geometry.

Polyhedral origami frames as topologically-defined interparticle linkers

Assembly of polyhedral origami frames was carried out using M13mp18 DNA and staple strands (1:10 ratio) in 1×TAE buffer with 12.5mM Mg²⁺, annealed slowly from 90 °C to a room temperature (see Supplementary Information). Proper assembly was confirmed using gel electrophoresis (Supplementary Fig. 1)⁴⁵, and negative-stained transmission electron microscopy (Supplementary Fig. 3). Cryo-electron microscopy (EM) with 3D reconstruction, as described previously⁴⁶, was also applied to visualize the assembled DNA frames (Supplementary Fig. 4–7). We probed the ability of the frame to coordinate nanoparticles, by creating frame-defined NP clusters. Gold nanoparticles (NPs) were coated with synthetic oligonucleotides, which are complimentary to the strands on the vertices of the frames (see Supplementary Information for the details of strand sequences). The NPs and DNA-frames were mixed in a ratio of 2.5N:1 (where N is the number of vertices for the frame) to form clusters^{31,32,46}. EM imaging, following purification with 1% agarose gel, demonstrated effective assembly of different cluster architectures (Supplementary Fig. 8–11), in which NPs are properly coordinated to the vertices of the corresponding polyhedral frames.

Next, we investigated the formation of extended 3D NP-DNA frameworks, in which the same kind of NP can be arranged into different types of lattices by providing differently-shaped connecting frames. We stress that the assembled NP-DNA framework might be or might not be crystalline. The formation of 3D ordered lattices of NPs (Fig. 1), is non-trivial: (i) if the particle size is significantly larger than frame dimensions, then a large number of frames can be attached to a particle, disrupting lattice topology; (ii) if NP size is too small, steric repulsion between frame edges will hinder hybridization of multiple frames to each particle; (iii) the length and rigidity of strands connecting vertices to NPs will influence the particle displacement and thus lattice order.

Nanoparticle-DNA framework assembly

We first discuss the assembly of a 3D lattice using an octahedral frame⁴⁶. To prepare the assembled system, DNA octahedra and NPs (10nm core) were mixed at the ratio of 1:2. To explore the role of particle-vertex linkages on the phase formation we studied the assembly behaviour as a function of the length, d , of the DNA motifs connecting the frame vertices to the NP. Partially-complementary single-stranded (ss) DNA strands extend from the octahedra vertices and particles respectively—so-called ‘sticky ends’—providing attachment of NPs to frames. We regulate the linking motif (denoted as $l-m-n$, see Table 1) by changing the number of oligonucleotides in both the non-complementary regions (l for frame vertex strand, n for NP) and the complementary overlap (m) of the complementary parts. The mixed solution of NPs and frames was annealed from 50 °C to 20 °C at 0.3 °C/h to insure the formation of thermodynamically equilibrium phases. Dark aggregates were observed at the bottom of the tube after the annealing process, indicating the appearance of a NP-octahedra condensed phase.

We first probed the internal structures of these aggregates (systems I–V) by *in-situ* Small-Angle X-ray Scattering (SAXS). The 2D scattering patterns and the corresponding structure

factors, $S(q)$, where q is the scattering vector, are shown in Fig. 2a. Remarkably, the system II (motif 2–6–10) revealed about thirty orders of resolution-limited Bragg peaks (Fig. 2a, $S(q)$ green curve), which signifies an high degree of long-range order. The use of either shorter or longer NP linking motifs results in a significantly reduced correlation length for the order, as evidenced by the broadening of the scattering peaks, and the greatly-reduced intensity of the higher-order reflections. The peak positions (higher order peaks relative to the first peak) for system II (green curve, Fig. 2) exhibit the ratios

$q/q_1=1: \sqrt{4/3}: \sqrt{8/3}: \sqrt{11/3}:2 \dots$, which is expected for the face-centred-cubic (FCC) phase. Given the nominal 1:2 stoichiometry of octahedra to NP, we indeed expect an FCC arrangement, as shown on the Fig. 2b. In this arrangement, the in-plane (equatorial) vertices (four corners) bind four nanoparticles, while each nanoparticle within this layer also binds four octahedra. Thus, a square NP pattern is established in the plane formed by the octahedron equatorial vertices (top view; see Fig. 2b, central panel). Consequently, these octahedra layers are connected by the out-of-plane (axial) vertices through another nanoparticle that binds only two octahedra form the lower and higher layers (side view, Fig. 2b, right panel).

To verify the formation of a FCC lattice (Fig. 3a1), we quantitatively modelled^{47,48} $S(q)$. Fig. 3a2 displays a 3D model of an individual octahedral frame, reconstructed using cryo-EM⁴⁶. It reveals that the edge length is around 29 nm, which agrees with the designed parameters of octahedral frame (28.6 nm for 84 base pairs edge). The experimental $S(q)$ for system II (Fig. 3a3, blue line) matches well the calculated scattering profile for an FCC lattice (Fig. 3a3, red line, see Supplementary Information for the details of scattering analysis). Importantly, not only do the calculated peak positions exactly match, but also the heights of the $S(q)$ peaks are in excellent agreement between data and model, supporting the proposed lattice and demonstrating the precise positioning of NP in the self-assembled lattice. The SAXS-determined FCC lattice constant is 67.7 nm at the room temperature, which is also in accordance with the design, 64.6 nm, considering the length of the octahedron edge and estimated sizes of NP and DNA shells.

Although the positions of nanoparticles in the lattices can be determined from SAXS data, the exact placement of DNA frames cannot be extracted in these measurements due to their low electron density in comparison with gold NPs, which dominates the scattering signal. Therefore, we performed stoichiometric study to find the ratio of frames to NP in assembled lattice (see details in Supplementary Information). We stress that the obtained frame-to-NP ratios for the assembled lattices and the SAXS determined placement of NPs in the lattices are the experimental basis for proposing the suitable frame arrangements for all systems shown in this work, and the future studies might further refine those arrangements. For the assembled lattice of octahedra frames and NPs our experiment shows that at the ratio of frame to NP is about 1:2; moreover, the lattice structure does not depend on the nominal mixing ratio (Supplementary Fig. 26). Thus, for this lattice we propose the frames arrangement (Fig. 3a4 and Supplementary Fig. 14 for enlarged view) that is symmetric and mechanically stable, and it satisfies the determined 1:2 ratio of frames to NPs and the observed FCC lattice of NPs. In the FCC lattice, as shown for the unit cell in Fig. 2b (left panel) and the large-scale view in Fig. 3a4, the octahedron vertices has two different binding

modes with nanoparticles: one is in the plane of equatorial vertices (four octahedra per particle), and the second mode is along axial vertices (two octahedra per particle). Notably, if the linker motif is too short (system I), the lattice formation is hindered because particles might be mis-centred within the vertex cavity; in addition, the edges of neighbouring octahedra might be in the unfavourable proximity. On other hand, if motifs are too long (systems III-V) the excessive flexibility of the connections deteriorates the order. Both scenarios were observed experimentally (Fig. 2a and Table 1).

Enabling lattice types by shaping polyhedral frames

We applied the demonstrated strategy towards the creation of other lattice symmetries, based on other frame geometries: cube, prism, elongated square bipyramid (ESB), and triangular pyramid (TBP). Following the successful construction of the FCC lattice for octahedron frames, we explored the assembly of “stretched” octahedral (ESB) frames with 10 nm NPs (ESB/NP ratio of about 1:2, same linker motifs and annealing protocol as described above). Fig. 3b2 and Supplementary Fig. 5 show the reconstructed 3D model from cryo-EM images, which confirm the correct assembly of ESB DNA frame and, consequently, the coordination of NPs in the ESB-frame defined cluster (Supplementary Fig. 9). The length of eight edges above and below the mid-plane is 1.25 times longer than the other four in-plane ones. This simple modification of the frame shape acts as a stringent test of our ability to manipulate the lattice structure via rational frame design. Moreover, it allows generating lower-symmetry unit cells, in which bases are not equal; *i.e.* the lattice parameter c in the cubic Bravais lattice will be different from a and b . This type of structure has not been reported for DNA-NP systems; moreover, such special low-symmetry arrangements are quite rare for spherical particles.

ESB-NP systems with appropriate motifs (Table 1) exhibit well-defined scattering peaks in $S(q)$, as shown in Fig. 3b3. The peak positions and relative intensities for this ESB-NP framework differ markedly from the $S(q)$ of octahedra-NP FCC lattice (Fig. 3a3). Peak indexing and detailed modelling reveal the structure to be a body-centred-tetragonal lattice (BCT), shown in Fig. 3b4. The modelled $S(q)$ (Fig. 3b3, red line, and see Table 1) is in a good agreement with the experimental data (Fig. 3b3, blue line). Indeed, for this unit cell $a=b < c$ (Table 1), which is consistent with our lattice “engineering” expectation. Interestingly, the lattice with non-equal bases might have implications for a distortion of a particle DNA shell, as we discuss below.

We next designed a cubic DNA frame, with edge lengths similar to the octahedra (Fig. 3c1). Intriguingly, most of the individual non-linked cubes are significantly skewed, as revealed by cryo-EM images and representative 2D class projection (Fig. 3c2 and Supplementary Fig. 5). Since this effect is observed only for cube frames, it might be attributed to the intrinsic flexibility associated with a cubic truss. Therefore, it is quite remarkable that, when assembled with 10 nm NPs, these flexible frames form an exceptionally ordered lattice (Fig. 3c3). The SAXS structure factor exhibits nearly thirty peaks at the position of $q/q_1=1: \sqrt{2}: \sqrt{3}: 2 \dots$, which is in excellent agreement with the calculated $S(q)$ profile for a simple cubic (SC) lattice (red line in Fig. 3c3) with the interparticle distance of 48.3 nm, in agreement with the designed estimation. Moreover, the excellent correspondence between

experimental and simulated curves again points towards the extreme order preserved over many lattice repeats. Considering the measured ratio of 1:2 of frames to NPs in the superlattice (see Supplementary Information), we propose the arrangement of cubic frames in SC lattice as shown in Fig. 3c₄ (see Supplementary Fig. 16 for enlarged model illustration). Such organization satisfies the requirements on the frame to NP ratio, exhibits higher symmetric and mechanical stability in comparison to other considered organizations (Supplementary Fig. 27). Moreover, the proposed organization minimizes edge-to-edge repulsion of neighbouring frames: only a pair of frame edges is in close proximity between the two neighbouring NPs, while each NP binds four different cubic frames. Interestingly, the absence of skew in the lattice suggests that there is a certain synergistic “correcting” effect of eight cubes linked to a single NP, and eight particles linked to each cubic frame; the uniform “pull” of all cubic edges in all directions stabilizes the network. Indeed, the NP cluster formed by particles attached to the vertices of cube frame shows low distortion (Supplementary Fig. 10). We also note that recent theoretical work predicted that non-floppy lattice arrangements provides greater mechanical stability⁴⁹.

The polyhedral frames discussed above have relatively high symmetry, with all faces equivalent (equilateral triangle for octahedron and ESB; squares for cube). We extended our approach to include lower-symmetry frames, such as a prism (Fig. 3d₁). The prism has two triangular and three square faces, which might hinder crystal formation due to the complicating factor of frame orientations. Nevertheless, the SAXS measurements for the assembled structure of prism frames and NPs (following the mixing and annealing procedures described above) revealed the formation of well-ordered lattice with about twenty recognizable $S(q)$ peaks (Fig. 3d₃, blue line). By examining the possible models for the assembled framework and considering the ratio of prisms and NPs in the superlattice, we found that a simple hexagonal (SH) lattice (Fig. 3d₄) agrees with the experimental $S(q)$. We examined different possibilities for prism frames arrangement considering the experimentally estimated ratio (1:2) of frames to NPs and observed SH lattice of NP. We suggest the model (Fig. 3d₄) that satisfied these requirements. In this lattice (see Supplementary Fig. 17 for the enlarged view), every particle binds three prisms, one on one side of particle hemisphere and two prisms on the other side. Thus, a layer of hexagonally arranged NPs is formed due to the triangular linking geometry of each prism bases, and those layers are stacked on top of each other because of the rectangular shape of lateral faces of the prism. To reduce the repulsion between DNA bundles for the given SH lattice and measured frame:NP ratio, the prisms’ arrangement in different layers is suggested to follow A-B-A stacking of prisms (A) and voids (B). For this framework, we found that $a=b < c$ ($a=b=71.1\text{nm}$ and $c=61.9$), and $\alpha=\beta=90^\circ$, while $\gamma=120^\circ$. We note that lattices with unequal bases, such as those built with ESB and prism frames show a larger deviation from the calculated frame dimensions than those with equal bases, like built with octahedron and cube frames. This effect is probably caused by the differences in binding modes between a frame and NP. For example, the number and location of particle bound frames might depend on the node location within the framework. Consequently, that can result in some deformation of the DNA shells of particles, and the frames themselves.

We investigated the assembly of NPs using triangular bipyramid (TBP) frames. These systems did not exhibit crystalline superlattices for any of the investigated linking motifs

(see Supplementary Table 2 for details and Supplementary Fig. 18). The crystallization in this case may be problematic due to the kinetic trapping and complex ground state. Additionally, TBP was computationally predicted to yield quasi-crystals over a wide range of TBP vertex truncations⁵⁰. Thus, it is quite possible that the observed amorphous organization of NP-TBP system is related to this aspect of TBP geometry.

Direct imaging of nanoparticle lattices

Next, we complemented the ensemble-averaged representation of lattices, as obtained from scattering studies, with a local probing of nanoparticle arrangements in the assemblies by applying a cryo-electron microscopy. The assembled structures were frozen with its native solution by plunging the sample into the nitrogen-cooled liquid ethane, following by imaging with an annular dark-field scanning transmission electron microscope (ADF-STEM) (see Supplementary Information). In this imaging mode, gold particles appear higher in intensity than the surrounding ice. We show in Fig. 4 the representative cryo-STEM images for two types of STEM-studied lattices, assembled with cubic and BCT frames (see also Supplementary Fig. 23–25). Due to the random orientation of crystallites in ice, different lattice projections can be observed. Fig. 4a₁ illustrates the observed projection of (111) plane for the simple cubic lattice, which agrees well with the shown lattice model (top left), and particle arrangements (top right). The nearest neighbour interparticle distance obtained from STEM is 40.2 nm, matching well the SAXS result (39.4nm). The tilted (100) projection for this lattice (shown in Fig. 4a₂) also demonstrates a good agreement between interparticle distances (from untitled direction) obtained from STEM, 50.7 nm, and SAXS, 48.3nm. For the BCT lattice assembled with elongated octahedra, two different projections are shown in Fig. 4b₁, (111), and Fig. 4b₂, (100). The (111) projection indicates that each imaged NP is surrounded by six neighbours, while four of them are closer than the other two. The STEM-measured nearest neighbour interparticle distance is 46.5nm, in agreement with SAXS-determined 47.0 nm. For (100) projection the observed interparticle distance, 53.2nm, also in close correspondence with the SAXS result, 52.5nm. Thus, our direct microscopic observations confirm the structure of assembled lattices and interparticle distances, and crystallites sizes determined by scattering method. Furthermore, the probing using a real-space imaging allows examining the presence of defects and vacancies in the lattice, which is difficult to reveal using scattering methods. The microscopic images (Fig. 4 and S23–25) indicate the lattice integrity within the crystalline domains, with a very low number of vacancies.

Outlook

Our results show that the proposed approach allow organizing the same particles into different crystallographic lattices, where the lattice types are determined by the shapes of used interparticle connecting frames (Table 1). Since the binding of frames to particles occur via vertices, the geometry of frames has a profound effect of the lattice type. This is because the assembly is driven by maximization of particle-frame attachments, and the ideal lattice formation should satisfy all bonds for vertices, which translates the frame geometry to the particular lattice type. We note that particles should not be significantly larger than frames. Otherwise the effect of frame geometry will be diminished. On the other side, topological

connections between particle and frames should be realized in the way that reducing the inter-frame repulsion. This can be achieved by separating frame attachment spots on particle surfaces via the choice of particle sizes and/or linking motifs between vertex and the particle surface. Moreover, as we demonstrated, the systems can also choose the appropriate ratio of frames in order to minimize the repulsion, but still maintain the lattice. That reflects the balance between lattice stabilizing factors (NP-frame bonds), inter-frame repulsion and entropic effects.

We summarize in Table 1 the effect of the frame-nanoparticle linking motifs on the lattice formation. The crystallization favours the greatest number of frame-NP bonds, and entropic gains associated with arrangements of shaped frames. However, the repulsion between frame edges and steric constraints can impose restrictions on the topology of connections provided by frames, and that can hamper the lattice formation. Indeed, we observed both effects by changing the length of the frame-NP binding motif. We first note that for our systems, each particle can accommodate more than 10 frames, based on simple area estimation. However, in reality, a much smaller number of frames are attached to particles in lattices, which is due to inter-frame repulsion, as we discussed above. Furthermore, in this case, short frame-NP linking motifs will result in close proximity of edges of neighbouring frames (see Supplementary Fig. 14–17) and that can destabilize the structure. On other side, the excessive flexibility of frame-NP bonds will mask the frame shape, i.e. the frame geometry cannot be translated effectively to the particle organization, and that leads again to the amorphous state. Besides, our experiments (see Supplementary Fig. 21–22) confirm that in order to maintain the topological connectivity required for a given symmetry of unit cell, particle diameter (including DNA shell) should be smaller than the frame dimensions. To fully develop the “engineering” methodology for the creation of desired lattices, the detailed computational and theoretical investigations are required. The future studies will shed light on the mechanism of lattice formation, on the precise positions of frames in the lattices and they might establish a direct correspondence between the frame geometry and the lattice symmetry.

We stress that engineering of lattices using the presented approach can be extended beyond the demonstrated examples of using vertices of polyhedral frame to connect particles into frameworks. For example, we envision several elaborations of our approach: (i) frame can be encoded to accommodate particles not only at vertices, but also at arbitrary positions within the frame, (ii) more than one type of particle can be incorporated, using corresponding DNA encoding of particles and their anchoring points on a frame (iii) the combination different frame shapes will permit creating a more complicated designed unit cells.

Methods

Design of polyhedral DNA origami frames

DNA origami polyhedral frames were designed using caDNAno software (<http://cadnano.org/>). Each edge of the frames is composed of a six-helix-bundle (6HB). For octahedral and cubic frames, the length of each 6HB is 28.6nm (84 base pairs); for prism and triangular bipyramid (TBP), the length of the 6HB is 42.8nm (126 base pairs); for elongated square bipyramid (ESB), the length for four edges in the mid-plane is 28.6nm

while the other eight edges have a length of 35.7nm (105 base pairs). One single-stranded DNA chain (sticky-end) at the each end of 6HB is designed to be complementary to the DNA attached to gold nanoparticle. For octahedron and ESB, there are four sticky ends each vertex; for cube and prism, there are three sticky ends each vertex; while for TBP, there are four sticky ends in vertices of the mid-triangle plane and three sticky ends in the two vertices above and below the mid-plane.

Folding of DNA Origami

DNA origami frames were prepared by mixing 10 nM scaffold DNA (M13mp18, Bayou Biolabs, LLC), 100 nM of each staple oligonucleotide in buffer solution which contains 1 mM EDTA, 12.5 mM MgCl₂, 5 mM Tris (pH=7.9 at 20°C). Then the mixture was rapidly heated from room temperature to 90 °C, maintained for 10 minutes, and followed by cooling down from 90 °C to 60 °C at the rate of 1°C/min, then 60°C to 20°C at the rate of 1°C/h to fold the target frames. Samples were then electrophoresed on 1% agarose gels (1× TBE, 10 mM MgCl₂, 0.5 µg/ml cyber gold) at 60 V for 2–3 h at room temperature, as shown in Figure S1.

Preparation of DNA-capped gold NPs

Gold nanoparticles (10 nm, 20 nm, 30 nm) functionalized with citric acid was purchased from Ted Pella Incorporated. Nanoparticles were modified with alkanethiol oligonucleotides by adding oligonucleotides to the aqueous nanoparticle solution at the mole ratio of 300:1 (DNA:NP, 1000:1 for 20nm NPs and 2000:1 for 30nm NPs) between DNA and NPs. After mixing for 2 hours, the solution was buffered at pH 7.4 (10 mM phosphate buffer). Salt (NaCl) was added gradually to the mixture until reaching the final concentration of 0.3M. 12 hours later, excessive reagents were removed by centrifugation for 60 min at 15,700rcf and washed 4 times with 0.1 M PBS buffer (0.1 M NaCl, 10 mM phosphate).

Preparation of DNA Frame/NP nanoclusters

In order to fabricate nanoclusters, 10nm (or 20nm, or 30 nm) gold NPs functionalized with the corresponding DNA sequences were added into the solution of DNA frames discussed above. The final ratio between the concentration of the NPs and frames depends on the number of vertices of the each frame; we used for assembly a ratio ($N_{\text{corner}} \times 2.5$):1, where N_{corner} is the number of vertices in the frame. The mixed solution was then annealed from 50°C to room temperature with a rate of 3°C/h, incubated overnight and concentrated by a 100K column (Millipore Cooperation). The obtained samples with red colour were then electrophoresed on 1% agarose gels (1× TBE, 10 mM MgCl₂, 0.5 µg/ml cyber gold) at 60 V for 3 h as shown in Figure S12. The target bands on the gel were cut, purified by a cellulose-acetate spin column (Bio-rad Cooperation) and ready for use.

Preparation of NP-DNA frameworks

For the preparation of the NP-DNA frameworks, the DNA frames of corresponding shapes and NPs were mixed, and then slowly cooled down from 50 °C to room temperature at the rate of 0.3°C/h. Buffer conditions in the frameworks are the same as the condition when folding the origami structures: 1×TAE, 12.5mM Mg²⁺. Black with tiny red aggregation was

found at the bottom of the tubes and the above solution was clear with no colour. Then the aggregations were transferred to the quartz capillary with the same buffer. These aggregates were investigated by in-situ SAXS to identify the internal structure, lattice type and degree of order for all studied frame shapes and NP-frame linking DNA motifs.

Electron microscopy

The carbon-coated grids were glow discharged in a 0.39 mbar air atmosphere for 1 min by using PELCO easiGlow (Ted Pella, Inc.). Cryo-EM grids were prepared in an FEI Vitrobot IV at 20 °C with the relative humidity set to 90% and force set to 0. 3.5 μ l of DNA specimen was pipetted onto a freshly glow-discharged lacey carbon grid covered with an additional thin layer of continuous carbon film. The sample solution was incubated on EM grid for 3 min, blotted for 5 s before being plunged into liquid ethane that was pre-cooled by liquid nitrogen. The cryo-EM grids were then transferred to and stored in liquid nitrogen. The cryo-EM grids were transferred in liquid nitrogen into a Gatan 626 cryo-specimen holder and then inserted into the microscope. The specimen temperature was maintained below -170 °C during data collection. Cryo-EM imaging was performed in JEOL JEM-2010F TEM operating at 200 kV. Cryo-EM images were recorded in the low-dose mode ($15 \text{ e}^-/\text{\AA}^2$) at 30,000 \times or 40,000 \times microscope magnification on a Gatan UltraScan 4000 CCD camera (4,096 \times 4,096 pixel), corresponding to 3.52 or 2.64 \AA /pixel sampling at the specimen level.

Dynamic Light Scattering (DLS)

We conducted the dynamic light scattering measurements using Malvern Zetasizer ZS instrument at the back-scattering geometry (173°). It was equipped with a laser source (633nm) and a backscattering detector. For measuring the melting temperatures of each NP/frame assembly, we cooled down the samples (1 \times TAE buffer with 12.5mM Mg^{2+}) slowly in the chamber of the machine from 50 °C to room temperature. The dependence of measured aggregate size *v.s.* temperature was obtained.

Cryo-Scanning Transmission Electron Microscopy (STEM)

Sample vitrification was carried out in an FEI Vitrobot plunge-freezing device set to an operating temperature of 10 °C with 90% relative humidity and 0 force for the blotting pad. Three microliters of the sample were applied to the freshly glow-discharged EM grid (company&size); after 180 s, the grid was blotted for 0.5 s and plunged into the liquid nitrogen-cooled liquid ethane to prepare the cryo-sample. It was subsequently cryo-transferred to a cryogenic holder cooled down to liquid-nitrogen temperature. The sample was then imaged in a field-emission transmission electron microscope (JEOL 2100F) operated at 200 keV in an annular dark-field scanning transmission electron microscopy mode (ADF-STEM). In this imaging mode, spatial resolution is not reduced by the inelastic scattering events underwent in the sample. In contrast, these inelastically scattered electrons would render significant resolution loss due to the chromatic aberration of the conventional TEM imaging mode. Therefore, ADF-STEM is superior to conventional TEM when imaging through micron-thick ices.

Supplementary Material

Refer to Web version on PubMed Central for supplementary material.

Acknowledgments

We thank W. Shih and Y. Ke for the help with DNA octahedra design and useful discussions. We thank L. Bai for the help with the cryo-STEM sample preparations. We thank D. Chen for assistance with schematic drawing. Research carried out at the Centre for Functional Nanomaterials, Brookhaven National Laboratory was supported by the U.S. Department of Energy, Office of Basic Energy Sciences, under Contract No. DE-SC0012704. H.L and T.W. were supported by National Institute of Health R01 grant (AG029979).

References

1. Talapin DV, Lee J-S, Kovalenko MV, Shevchenko EV. Prospects of Colloidal Nanocrystals for Electronic and Optoelectronic Applications. *Chem. Rev.* 2010; 110:389–458. [PubMed: 19958036]
2. Hu T, Isaacoff BP, Bahng JH, Hao C, Zhou Y, Zhu J, Li X, Wang Z, Liu S, Xu C, Biteen JS, Kotov NA. Self-Organization of Plasmonic and Excitonic Nanoparticles into Resonant Chiral Supraparticle Assemblies. *Nano Lett.* 2014; 14:6799–6810. [PubMed: 25400100]
3. Cargnello M, Johnston-Peck AC, Diroll BT, Wong E, Datta B, Damodhar D, Doan-Nguyen VVT, Herzing AA, Kagan CR, Murray CB. Substitutional doping in nanocrystal superlattices. *Nature.* 2015; 524:450–453. [PubMed: 26310766]
4. Kuzyk A, Schreiber R, Fan Z, Pardatscher G, Roller E-M, Högele A, Simmel FC, Govorov AO, Liedl T. DNA-based self-assembly of chiral plasmonic nanostructures with tailored optical response. *Nature.* 2012; 483:311–314. [PubMed: 22422265]
5. Xiong H, Sfeir MY, Gang O. Assembly, structure and optical response of three-dimensional dynamically tunable multicomponent superlattices. *Nano Lett.* 2010; 10:4456–4462. [PubMed: 20879781]
6. Alder BJ, Wainwright TE. Phase transition for a hard sphere system. *J. Chem. Phys.* 1957; 27:1208–1209.
7. Zhu JX, Li M, Rogers R, Meyer W, Ottewill RH, Russell WB, Chaikin PM. Crystallization of hard-sphere colloids in microgravity. *Nature.* 1997; 387:883–885.
8. Casey MT, Scarlett RT, Rogers WB, Jenkins I, Sinno T, Crocker JC. Driving diffusionless transformations in colloidal crystals using DNA handshaking. *Nat. Commun.* 2012; 3:1–8.
9. Travesset A. Binary nanoparticle superlattices of soft-particle systems. *Proc. Natl. Acad. Sci. U.S.A.* 2015; 112:9563–9567. [PubMed: 26195799]
10. Kranendonk WGT, Frenkel D. Simulation of the adhesive-hard-sphere model. *Mol. Phys.* 1988; 64:403–424.
11. Damasceno PF, Engel M, Glotzer SC. Predictive self-assembly of polyhedra into complex structures. *Science.* 2012; 337:453–457. [PubMed: 22837525]
12. Leunissen ME, Christova CG, Hynninen AP, Royall CP, Campbell AI, Imhof A, Dijkstra M, van Roij R, van Blaaderen A. Ionic colloidal crystals of oppositely charged particles. *Nature.* 2005; 437:235–240. [PubMed: 16148929]
13. Shevchenko EV, Talapin DV, Kotov NA, O'Brien S, Murray CB. Structural diversity in binary nanoparticle superlattices. *Nature.* 2006; 439:55–59. [PubMed: 16397494]
14. Nykypanchuk D, Maye MM, van der Lelie D, Gang O. DNA-guided crystallization of colloidal nanoparticles. *Nature.* 2008; 451:549–552. [PubMed: 18235496]
15. Park SY, Lytton-Jean AKR, Lee B, Weigand S, Schatz GC, Mirkin CA. DNA-programmable nanoparticle crystallization. *Nature.* 2008; 451:553–556. [PubMed: 18235497]
16. Auyeung E, Cutler JJ, Macfarlane RJ, Jones MR, Wu J, Liu G, Zhang K, Osberg KD, Mirkin CA. Synthetically programmable nanoparticle superlattices using a hollow three-dimensional spacer approach. *Nat. Nanotechnol.* 2012; 7:24–28.

17. Talapin DV, Shevchenko EV, Bodnarchuk MI, Ye X, Chen J, Murray CB. Quasicrystalline order in self-assembled binary nanoparticle superlattices. *Nature*. 2009; 461:964–967. [PubMed: 19829378]
18. Rechtsman MC, Stillinger FH, Torquato S. Synthetic diamond and wurtzite structures self-assemble with isotropic pair interactions. *Phys. Rev. E*. 2007; 75:031403.
19. Jain A, Errington JR, Truskett TM. Dimensionality and design of isotropic interactions that stabilize honeycomb, square, simple cubic, and diamond lattices. *Phys. Rev. X*. 2014; 4:031049.
20. Tkachenko AV. Morphological diversity of DNA-colloidal self-assembly. *Phys. Rev. Lett.* 2002; 89:148303. [PubMed: 12366080]
21. Angioletti-Uberti S, Varilly P, Mognetti BM, Frenkel D. Mobile linkers on DNA-coated Colloids: valency without patches. *Phys. Rev. Lett.* 2014; 113:128308.
22. Glotzer SC, Solomon MJ. Anisotropy of building blocks and their assembly into complex structures. *Nat. Mater.* 2007; 6:557–562. [PubMed: 17667968]
23. Jones MR, Macfarlane RJ, Lee B, Zhang J, Young KL, Senesi AJ, Mirkin CA. DNA-nanoparticle superlattices formed from anisotropic building blocks. *Nat. Mater.* 2010; 9:913–917. [PubMed: 20890281]
24. Zhang Y, Lu F, Lelie Dvd, Gang O. Continuous phase transformation in nanocube assemblies. *Phys. Rev. Lett.* 2011; 107:135701. [PubMed: 22026873]
25. Xiong HM, van der Lelie D, Gang O. Phase behavior of nanoparticles assembled by DNA linkers. *Phys. Rev. Lett.* 2009; 102:015504. [PubMed: 19257208]
26. van Anders G, Ahmed NK, Smith R, Engel M, Glotzer SC. Entropically patchy particles: engineering valence through shape entropy. *ACS Nano*. 2014; 8:931–940. [PubMed: 24359081]
27. Macfarlane RJ, Lee B, Jones MR, Harris N, Schatz GC, Mirkin CA. Nanoparticle superlattice engineering with DNA. *Science*. 2011; 334:204–208. [PubMed: 21998382]
28. Paik T, Murray CB. Shape-directed binary assembly of anisotropic nanoplates: a nanocrystal puzzle with shape-complementary building blocks. *Nano Lett.* 2013; 13:2952–2956. [PubMed: 23668826]
29. Romano F, Sanz E, Sciortino F. Phase diagram of a tetrahedral patchy particle model for different interaction ranges. *J. Chem. Phys.* 2010; 132:184501.
30. Russo J, Tartaglia P, Sciortino F. Association of limited valence patchy particles in two dimensions. *Soft Matter*. 2010; 6:4229–4236.
31. Chen Q, Bae SC, Granick S. Directed self-assembly of a colloidal kagome lattice. *Nature*. 2012; 469:381–384.
32. Wang Y, Wang Y, Breed DR, Manoharan VN, Feng L, Hollingsworth AD, Weck M, Pine DJ. Colloids with valence and specific directional bonding. *Nature*. 2012; 491:51–56. [PubMed: 23128225]
33. Lu F, Yager KG, Zhang Y, Xin H, Gang O. Superlattices assembled through shape-induced directional binding. *Nat. Commun.* 2015; 6:1–10.
34. O'Brien MN, Jones MR, Lee B, Mirkin CA. Anisotropic nanoparticle complementarity in DNA-mediated co-crystallization. *Nat. Mater.* 2015; 14:833–839. [PubMed: 26006002]
35. Edwardson TGW, Carneiro KMM, McLaughlin CK, Serpell CJ, Sleiman HF. Site-specific positioning of dendritic alkyl chains on DNA cages enables their geometry-dependent self-assembly. *Nat. Chem.* 2013; 5:868–875. [PubMed: 24056344]
36. Suzuki K, Hosokawa K, Maeda M. Controlling the number and positions of oligonucleotides on gold nanoparticle surfaces. *J. Am. Chem. Soc.* 2009; 131:7518–7519. [PubMed: 19445511]
37. Ye X, Millan JA, Engel M, Chen J, Diroll BT, Glotzer SC, Murray CB. Shape alloys of nanorods and nanospheres from self-assembly. *Nano Lett.* 2013; 13:4980–4988. [PubMed: 24044735]
38. Zheng JP, Birktoft JJ, Chen Y, Wang T, Sha RJ, Constantinou PE, Ginell SL, Mao CD, Seeman NC. From molecular to macroscopic via the rational design of a self-assembled 3D DNA crystal. *Nature*. 2009; 461:74–77. [PubMed: 19727196]
39. Rogers WB, Manoharan VN. Programming colloidal phase transitions with DNA strand displacement. *Science*. 2015; 347:639–642. [PubMed: 25657244]

40. Rothemund PWK. Folding DNA to create nanoscale shapes and patterns. *Nature*. 2006; 440:297–302. [PubMed: 16541064]
41. Douglas SM, Dietz H, Liedl T, Hogberg B, Graf F, Shih WM. Self-assembly of DNA into nanoscale three-dimensional shapes. *Nature*. 2009; 459:414–418. [PubMed: 19458720]
42. Zhao Z, Jacovetty EL, Liu Y, Yan H. Encapsulation of gold nanoparticles in a DNA origami cage. *Angew. Chem. Int. Ed.* 2011; 50:2041–2044.
43. Schreiber R, Do J, Roller E-M, Zhang T, Schüller VJ, Nickels PC, Feldmann J, Liedl T. Hierarchical assembly of metal nanoparticles, quantum dots and organic dyes using DNA origami scaffolds. *Nat. Nanotechnol.* 2014; 9:74–78. [PubMed: 24292513]
44. Seeman NC. Nucleic-acid junctions and lattices. *J. Theor. Biol.* 1982; 99:237–247. [PubMed: 6188926]
45. Douglas SM, Marblestone AH, Teerapittayanon S, Vazquez A, Church GM, Shih WM. Rapid prototyping of 3D DNA-origami shapes with caDNAno. *Nucleic Acids Res.* 2009; 37:5001–5006. [PubMed: 19531737]
46. Tian Y, Wang T, Liu W, Xin HL, Huilin Li, Ke Y, Shih WM, Gang O. Prescribed nanoparticle cluster architectures and low-dimensional arrays built using octahedral DNA origami frames. *Nat. Nanotechnol.* 2015; 10:637–644. [PubMed: 26005999]
47. Yager KG, Zhang YG, Lu F, Gang O. Periodic lattices of arbitrary nano-objects: modeling and applications for self-assembled systems. *J. Appl. Crystallogr.* 2014; 47:118–129.
48. Zhang YG, Pal S, Srinivasan B, Vo T, Kumar S, Gang O. Selective transformations between nanoparticle superlattices via the reprogramming of DNA-mediated interactions. *Nat. Mater.* 2015; 14:840–847. [PubMed: 26006003]
49. Mao X, Souslov A, Mendoza CI, Lubensky TC. Mechanical instability at finite temperature. *Nat. Commun.* 2014; 6:1–8.
50. Haji-Akbari A, Chen ER, Engel M, Glotzer SC. Packing and self-assembly of truncated triangular bipyramids. *Phys. Rev. B.* 2013; 88:012127.

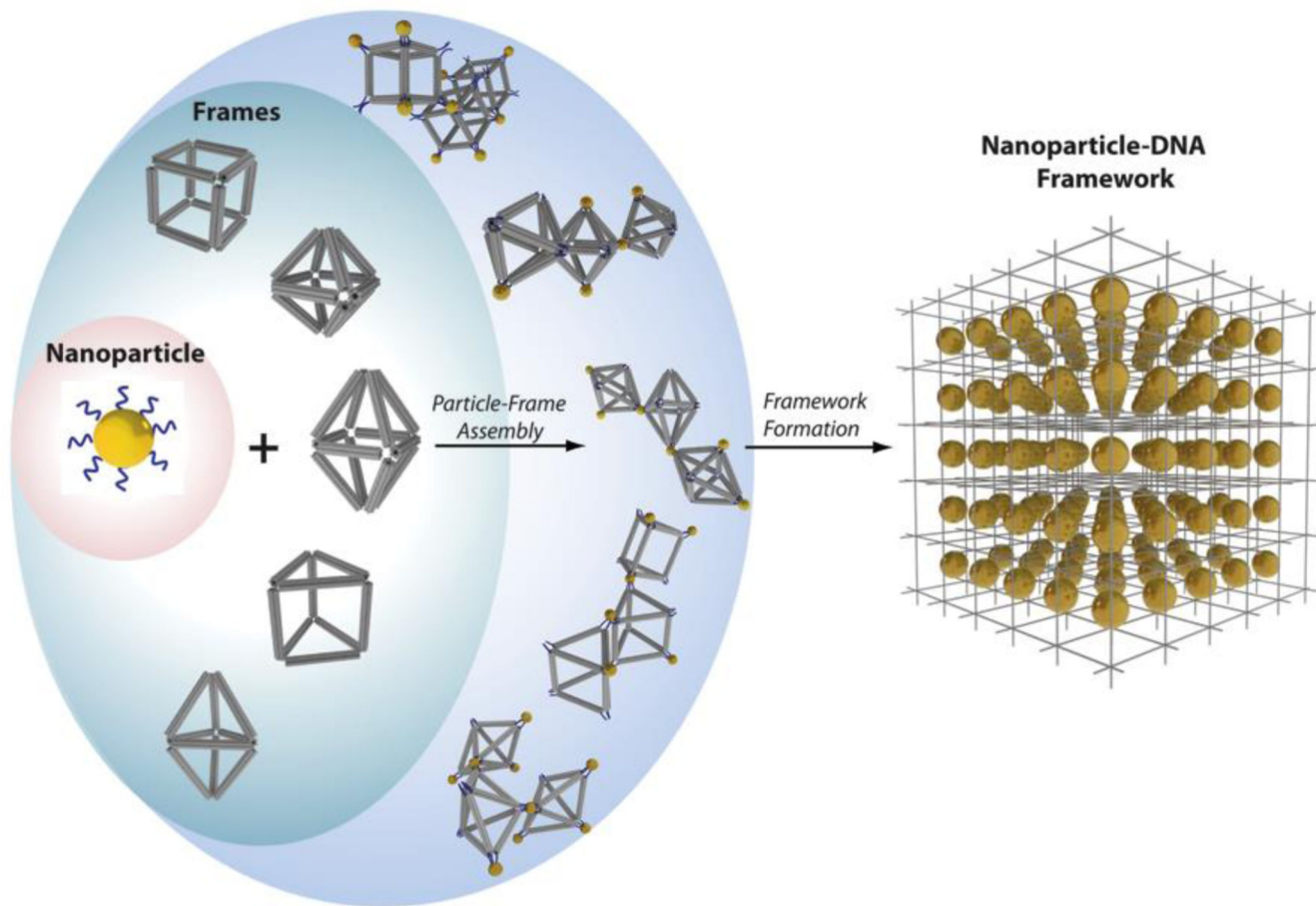


Figure 1. Lattice assembly via Nanoparticle-DNA Framework

Nanoparticles (NPs) (yellow ball) capped with oligonucleotides (blue curves) are mixed with polyhedral DNA frames (from top to bottom): cube, octahedron, elongated square bipyramid (ESB), prism, triangular bipyramid (TBP). The frames are designed to have complementary strands at the vertices for NP binding. An aggregation (framework formation) is expected when NPs and the correspondingly encoded polyhedral frames are allowed to mix and hybridize. NP-DNA Frameworks might exhibit ordered lattice for optimized NP sizes, linking motif, and annealing process. The crystallographic symmetry of the assembled lattice is controlled by the shape of interparticle linking frames, but not by the NPs themselves. This strategy thus enables “engineering” the lattice and its unit cell.

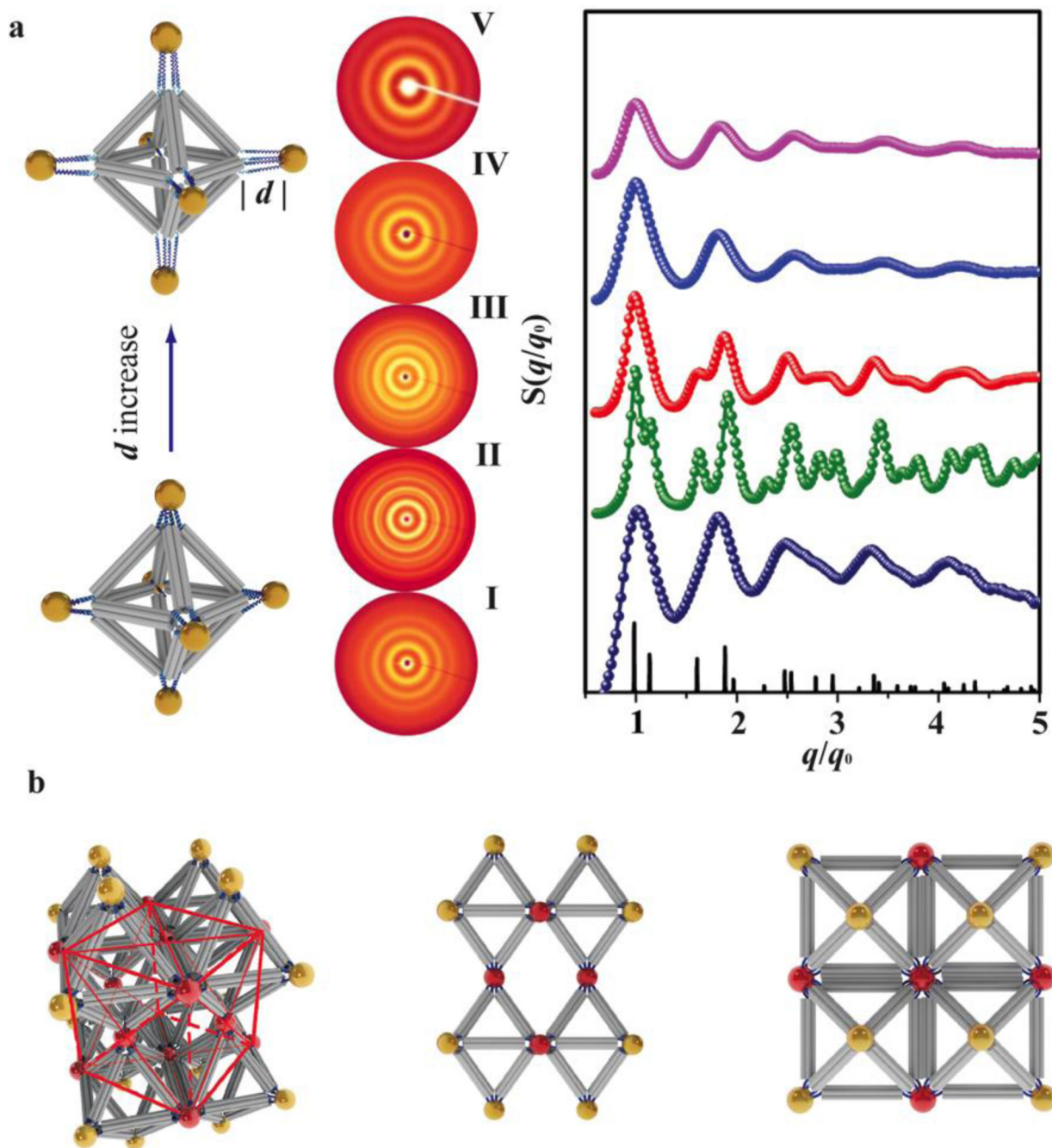


Figure 2. The formation of NP-DNA 3D lattice with octahedra frames and the effect of NP-vertex linker length

(a). The length of the linkers is increased (systems I to V, from bottom to the top) by changing the DNA linking motif. For respective systems (in parentheses) motifs are $0-6-10$ (I), $2-6-10$ (II), $9-6-10$ (III), $6-9-21$ (IV), $0-15-15$ (V), see also Table 1 and Supplementary Information. The central panel shows 2D SAXS data for each system. The corresponding structure factors $S(q/q_0)$ are shown (coloured lines/circles) on the right. The indexing of scattering peaks positions and intensities for FCC lattice is shown (black lines). (b).

Proposed assembled superlattice of NPs and octahedra. The particles within a single unit cell (marked by red lines) of FCC structure are shown in red on the left panel. The corresponding side and top views of the FCC structured NP-DNA framework are shown on the centre and right panels respectively.

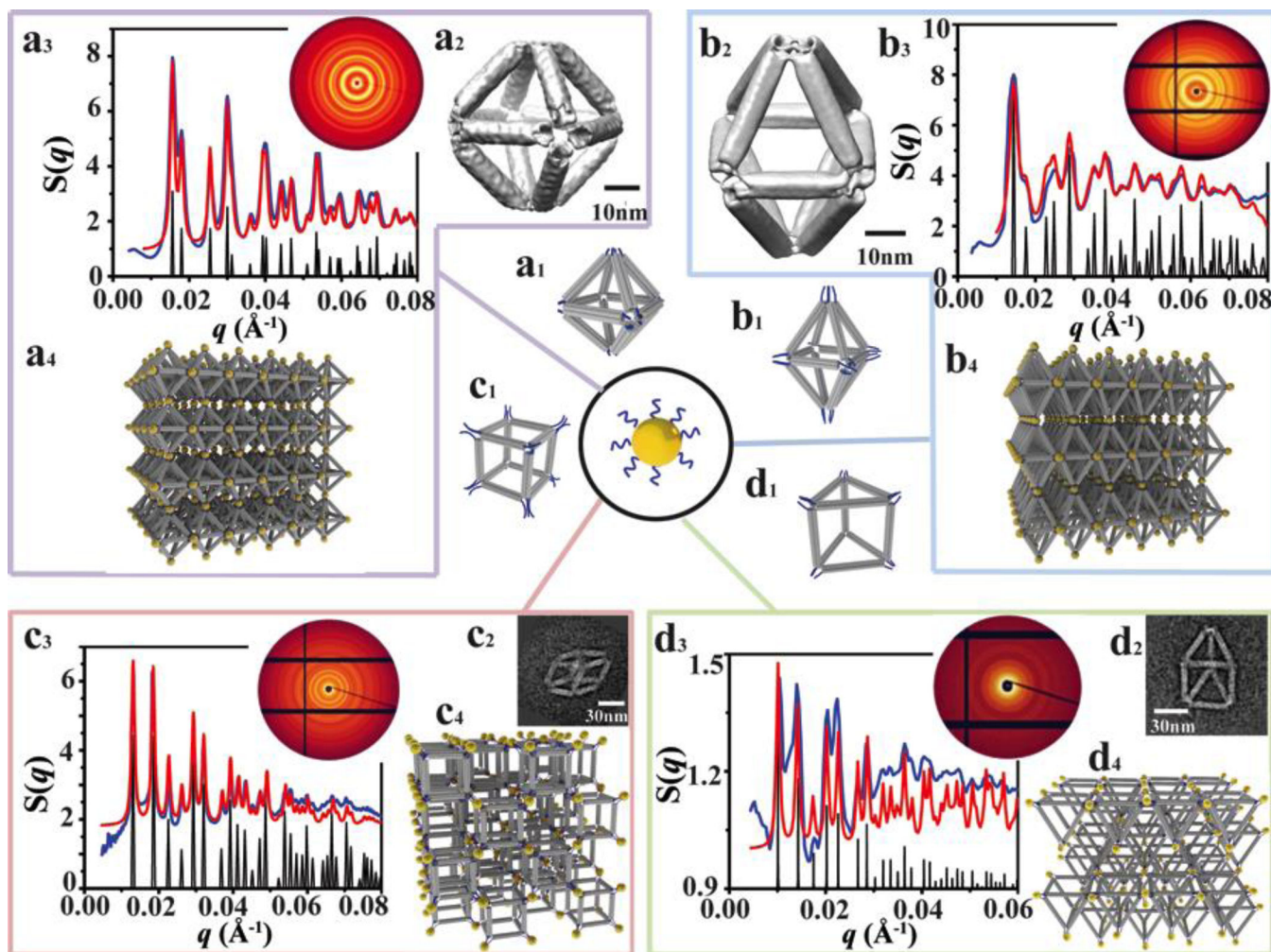


Figure 3. Nanoparticle superlattices assembled via DNA frames

(a – d) DNA-coated NPs (10 nm gold core) bound to four different types of frames via complementary DNA strands at their respective vertices. The four polyhedral frames are: octahedron (a_1), ESB (b_1), cube (c_1) and prism (d_1). For each, we show EM image (2) (see the Supplementary Information for the details of 3D reconstruction from cryo-TEM measurements), x-ray scattering structure factor, $S(q)$ with the 2D SAXS pattern as inset (3) were obtained in-situ after the annealing of the formed NP-DNA frameworks, and the proposed superlattice structures, as discussed in the text. See Supplementary Fig. 14–17 for the enlarged views of NP lattice models and the idealized arrangements of DNA frames for the obtained frames to NPs ratios, see the text (4). For each lattice structure, the experimental scattering profile is in blue and the model fitting in red. The black peaks mark the standard peak positions of the proposed lattice: FCC by the octahedra (a_3), BCT by ESB (b_3), simple cubic by the cubes (c_3), and hexagonal by the prisms (d_3).

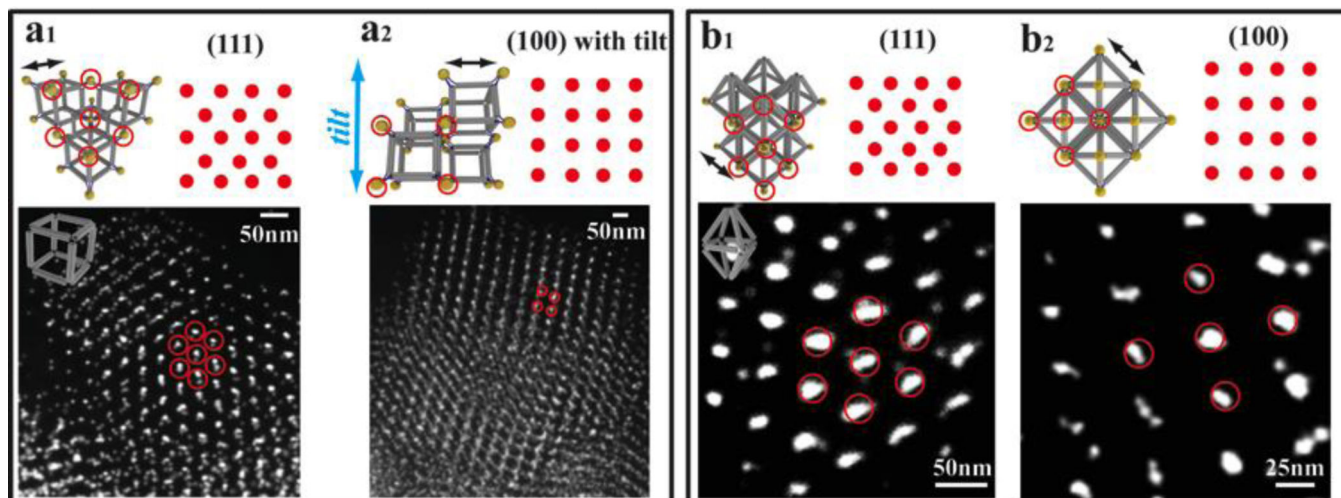
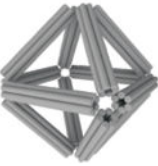
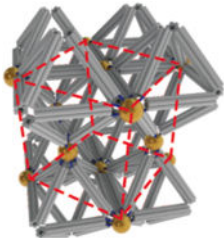

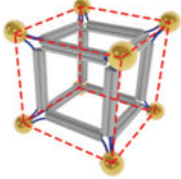

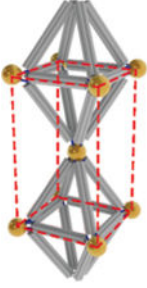

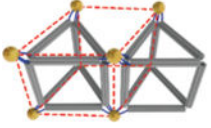



Figure 4. Cryo-STEM images for simple cubic (SC) (a_1 , a_2) and body centred tetragonal (BCT) (b_1 , b_2) lattices of NPs assembled with cubic and ESB frames, respectively
 (a_1) STEM image of the (111) plane projection for the SC lattice; the nearest interparticle distance is 40.2nm. (a_2) STEM image of the (100) face projection for the SC lattice which is tilted in one direction; the nearest interparticle distance is 50.7nm. (b_1) STEM image of the (111) face projection of the BCT lattice, the nearest interparticle distance is 46.5nm. (b_2) STEM image of the (100) face projection of the BCT lattice, the nearest interparticle distance is 53.2nm. The top left and right parts of each panel display the lattice model with the corresponding projection and the particle arrangements, respectively. The corresponding particles from the models and images are highlighted by red circles.

Table 1
The summary of designed and experimentally observed lattices based on Nanoparticle-DNA Frameworks

The different lattice types and disordered structures were obtained for the shown polyhedral DNA frames and the corresponding linking motifs. Lattice parameters, as obtained from the SAXS measurements and from the estimations (in parentheses) for the designed structures, are given. See the text and Supplementary Information for the details.

Frame Shape	Linker Motif, <i>l-m-n</i>	Lattice Type	Lattice parameters, experimental and (designed) values	Unit Cell
	0-6-10	Amorphous		
	2-6-10	<i>FCC</i>	$a=b=c=67.7$ (64.6) nm; $\alpha=\beta=\gamma=90^\circ$	
	9-6-10	<i>FCC</i>	$a=b=c=69.0$ (69.4) nm; $\alpha=\beta=\gamma=90^\circ$	
	6-9-21	Amorphous		
	0-15-15	Amorphous		
	9-6-10	Amorphous		
	6-9-21	<i>Simple Cubic</i>	$a=b=c=48.3$ (49.9) nm; $\alpha=\beta=\gamma=90^\circ$	
	0-15-15	Amorphous		
	2-6-10	<i>BCT</i>	$a=b=50.0$ (45.7) nm; $c=86.6$ (77.7) nm; $\alpha=\beta=\gamma=90^\circ$	
	9-6-10	<i>BCT</i>	$a=b=52.5$ (49.1) nm; $c=91.0$ (85.0) nm; $\alpha=\beta=\gamma=90^\circ$	
	6-9-21	Amorphous		
	2-8-22	Amorphous		
	2-8-32	<i>Simple Hexagonal</i>	$a=b=71.1$ (74.9) nm; $c=61.9$ (65.2) nm; $\alpha=\beta=90^\circ$; $\gamma=120^\circ$	
	Various designs (See SI)	Amorphous		